

LEFT: Learnable Fusion of Tri-view Tokens for Unsupervised Time Series Anomaly Detection

Dezheng Wang

wangdezheng@seu.edu.cn

School of Automation, Southeast University Nanjing, China

Tong Chen

tong.chen@uq.edu.au

School of Electrical Engineering and Computer Science, The University of Queensland Brisbane, Australia

Guansong Pang

gspang@smu.edu.sg

School of Computing and Information Systems, Singapore Management University Singapore

Congyan Chen*

Shihua Li

chency@seu.edu.cn

lsh@seu.edu.cn

School of Automation, Southeast University Nanjing, China

Hongzhi Yin*

h.yin1@uq.edu.au

School of Electrical Engineering and Computer Science, The University of Queensland Brisbane, Australia

Abstract

As a fundamental data mining task, unsupervised time series anomaly detection (TSAD) aims to build a model for identifying abnormal timestamps without assuming the availability of annotations. A key challenge in unsupervised TSAD is that many anomalies are too subtle to exhibit detectable deviation in any single view (e.g., time domain), and instead manifest as inconsistencies across multiple views like time, frequency, and a mixture of resolutions. However, most cross-view methods rely on feature or score fusion and do not enforce analysis–synthesis consistency, meaning the frequency branch is not required to reconstruct the time signal through an inverse transform, and vice versa. In this paper, we present Learnable Fusion of Tri-view Tokens (LEFT), a unified unsupervised TSAD framework that models anomalies as inconsistencies across complementary representations. LEFT learns feature tokens from three views of the same input time series: frequency-domain tokens that embed periodicity information, time-domain tokens that capture local dynamics, and multi-scale tokens that learn abnormal patterns at varying time series granularities. By learning a set of adaptive Nyquist-constrained spectral filters, the original time series is rescaled into multiple resolutions and then encoded, allowing these multi-scale tokens to complement the extracted frequency- and time-domain information. When generating the fused representation, we introduce a novel objective that reconstructs fine-grained targets from coarser multi-scale structure, and put forward an innovative time-frequency cycle consistency constraint to explicitly regularize cross-view agreement. As our

proposed unsupervised learning objectives effectively enable cross-view information exchange during model training, the tri-view encoders in LEFT can take advantage of a lightweight design. Experiments on real-world benchmarks show that LEFT yields the best detection accuracy against state-of-the-art baselines, while achieving a 5 \times reduction on FLOPs and 8 \times speed-up for training. Code is available at <https://github.com/DezhengWang/Left.git>

Keywords

Time Series Anomaly Detection, Unsupervised Learning, Cross-view Consistency, Tri-view Tokenization, Learnable Filterbank

ACM Reference Format:

Dezheng Wang, Tong Chen, Guansong Pang, Congyan Chen*, Shihua Li, and Hongzhi Yin*. 2026. LEFT: Learnable Fusion of Tri-view Tokens for Unsupervised Time Series Anomaly Detection. In . ACM, New York, NY, USA, 14 pages. <https://doi.org/10.1145/nnnnnnnnnnnnnnnn>

1 Introduction

Unsupervised time series anomaly detection (TSAD) is a core component in industrial systems, as the ability to generate early alarms on abnormal timestamps without annotated data can support safe operation and reduce maintenance and downtime cost [12, 19]. In real deployments, anomalies are heterogeneous: some are short transients, some are gradual drifts, and some mainly appear as changes in periodic structure and spectral energy [10, 38]. This heterogeneity renders a detector focusing on a single perspective unreliable, and motivates the extraction of multi-view information for unsupervised TSAD.

From a signal processing perspective, the time and frequency domains are linked by the Fourier transform, which provides a principled connection between these two views [45]. This connection motivates unsupervised TSAD methods to jointly use both views [17]: time-domain features capture local dynamics and abrupt deviations [39], while frequency-domain features highlight periodic irregularities and band-specific shifts that can be subtle or suppressed by noise in the raw data [46]. As such, by measuring the

Permission to make digital or hard copies of all or part of this work for personal or classroom use is granted without fee provided that copies are not made or distributed for profit or commercial advantage and that copies bear this notice and the full citation on the first page. Copyrights for components of this work owned by others than the author(s) must be honored. Abstracting with credit is permitted. To copy otherwise, or republish, to post on servers or to redistribute to lists, requires prior specific permission and/or a fee. Request permissions from permissions@acm.org.

Conference'17, Washington, DC, USA

© 2026 Copyright held by the owner/author(s). Publication rights licensed to ACM.

ACM ISBN 978-x-xxxx-xxxx-x/YY/MM

<https://doi.org/10.1145/nnnnnnnnnnnnnnnn>

disagreement between the representations learned from these two views, an anomaly score can be computed for each timestamp in an unsupervised fashion. However, most methods based on time and frequency views still operate on a single sampling resolution, where the model observes only one temporal granularity. Apart from restricting a model’s receptive field when learning time series representations, it also prevents the detector from explicitly verifying whether coarse structure (e.g., seasonality) and fine-grained dynamics (e.g., daily change) remain consistent. For example, a gradual drift, for example, can reshape the coarse trend while slightly detuning short-term rhythms [46]. In reality, abnormal traces can exhibit different patterns at different sampling granularities, and such anomalies can be hardly detected without inspecting such nuanced coarse-to-fine associations [10, 37].

In this regard, introducing multi-scale features at different sampling resolutions as an additional view is a natural enhancement to using only time and frequency features. Intuitively, by jointly modeling time-frequency alignment and cross-resolution consistency, a mutually complementary set of signals can be considered for TSAD. However, this brings an additional layer of complexity when learning useful anomaly detection signals from these views with varying semantics, and two significant challenges are to be addressed to maximize the utility of all views for unsupervised TSAD. We outline the challenges below.

Challenge 1: How to learn high-quality intra-view features without supervision signals? For time and frequency views, most TSAD methods fuse features or scores across both views, or align their feature spaces [6]. These designs rarely enforce Fourier-based consistency, meaning the predicted spectrum is not required to reconstruct the signal via an inverse transform, and the reconstructed signal is not required to match the spectrum under a forward transform [36]. This leaves the training process prone to learning a biased shortcut that only fits its own view, making cross-domain disagreement a less reliable indicator of true anomalies [6]. For the third view involving multi-scale feature encoding, its performance also hinges on the choice of sampling scales/granularities that are usually tuned via heuristics. However, in different time series data, regimes differ in dominant periods and noise, so the same setting can place the key periodic band at the wrong scale or mix it with noise and miss anomaly-related changes [38]. For example, in some time series with frequent fluctuations, performing straightforward downsampling on time series can fold fast oscillations into low frequencies, so a coarse-scale sequence may show a false flat trend created by aliasing rather than real long-range structure, distorting the learned representations [17, 43].

Challenge 2: How to align information from cross-view features for effective anomaly scoring on timestamps? Information fusion across three distinct views is expected to distil complementary information from time, frequency, and multi-scale structure, which enables coherence-based detection on anomalies. However, when generating anomaly scores for each timestamp, existing TSAD methods are restricted to considering either: (1) the disagreement between features extracted from time and frequency views; or (2) the disagreement across all data resolutions in the multi-scale view. Some works exploit time and frequency views through short-time Fourier transform (STFT) assisted by fusion or reconstruction objectives [6, 17], while others emphasize multi-scale features by learning

representations at diverse temporal resolutions and aggregating scale-wise outputs [10]. While often developed in parallel, few pipelines jointly model time, frequency, and explicit multi-scale characteristics of the same time series in a unified framework to facilitate effective anomaly scoring on timestamps [23].

Motivated by the above challenges, we propose **Learnable Fusion of Tri-view Tokens (LEFT)** for unsupervised TSAD, which treats anomalies as violations of agreement among time dynamics, time-frequency structure, and multi-scale structure. LEFT builds three complementary views and makes their agreement measurable. It enforces a bidirectional time-frequency cycle, so the time prediction must agree with the input spectrum after analysis and the spectrum prediction must reconstruct the input signal after synthesis. This analysis-synthesis coupling goes beyond feature or score fusion, reduces view-specific shortcuts, and makes time-frequency disagreement a more reliable anomaly evidence. For multi-scale structure, LEFT uses a Nyquist-constrained learnable filterbank with residual coverage, so it learns dataset-specific band allocations while band-limiting each scale before downsampling to control aliasing and avoid heuristic scale choices. The three token streams interact through selected lightweight fusion rather than dense all-pairs fusion, so the model aligns shared information without washing out view-specific evidence. Training further includes a cross-path consistency constraint that aligns the time-frequency cycle with the multi-scale reconstruction, and inference combines multi-scale residuals with cycle-based discrepancy signals to form the final anomaly score.

We summarize our contributions as follows:

- We formalize a unified tri-view setting that combines time dynamics, time-frequency structure, and multi-scale structure, where anomalies are exposed as violations of cross-view and cross-resolution consistency.
- We propose a Nyquist-constrained learnable filterbank with residual coverage to generate stable multi-scale structural tokens without fixed band partitions. We introduce a bidirectional time-frequency cycle consistency constraint to enforce analysis-synthesis agreement, and a cross-path consistency constraint to align the time-frequency pathway with multi-scale reconstruction. We also design lightweight token interactions to promote alignment without over-mixing, so view-specific evidence is preserved for anomaly scoring.
- Extensive experiments show consistent improvements over strong baselines, and demonstrate LEFT improves about 3% in VUS-ROC and 6% in VUS-PR, while reducing FLOPs by over 80% and speeds up training by about 8×.

2 Related Work

Unsupervised TSAD Unsupervised TSAD has been studied for decades, from classical pipelines to modern deep models [10, 25]. Classical methods such as LOF [3], DAGMM [49], and SVDD [32] are simple and cheap, but they can degrade on industrial data with non-stationary behavior, long-range dependence, and strong variable coupling [2]. Deep unsupervised TSAD is often grouped into forecasting, reconstruction, and self-supervised or contrastive methods [30, 42]. Attention-based models are widely used to capture long-range patterns and variable interactions [10, 14]. Anomaly

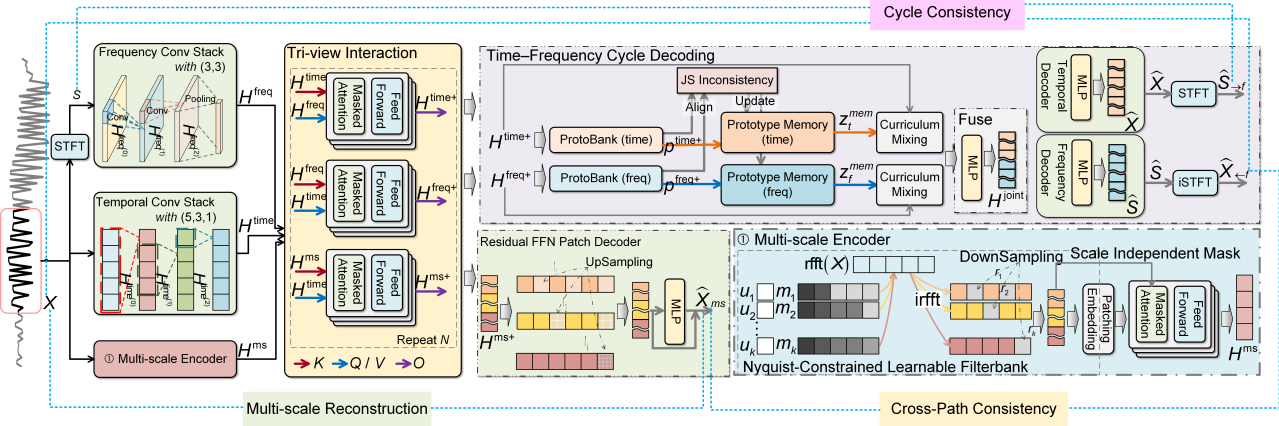


Figure 1: The architecture of LEFT.

Transformer detects anomalies via association inconsistency [41], while DCdetector uses discrepancy-aware contrastive learning [42].

Time-frequency modeling for unsupervised TSAD Because anomaly evidence can be weak in a single domain, many works incorporate time-frequency information to capture spectral changes such as periodic shifts and band-wise energy redistribution [9]. Common designs extract Fourier or wavelet features, or adopt frequency-aware architectures [37, 47]. In many cases, time and frequency are encoded in parallel and coupled through feature alignment or late fusion, which can underuse abnormal time-frequency coupling as a detection signal [17]. Empirical studies also suggest that single-scale time-domain sampling can miss anomaly signatures in time-frequency analysis [10].

Multi-scale modeling for unsupervised TSAD Multi-scale modeling addresses this issue by representing a series at multiple temporal resolutions. Recent work uses multi-resolution tokenization, patching, or scale mixing [5, 18, 34], and TimesNet models multiple period-based views [37]. In TSAD, multi-scale methods often use per-scale experts with late fusion or shared backbones with implicit scale mixing [27, 44]. Yet anomalies may remain weak at any single resolution and become clearer when coarse structure and fine dynamics stop aligning, which motivates more explicit cross-scale modeling [10, 46]. At the same time, many multi-scale pipelines focus on time-domain representations and do not explicitly integrate frequency-domain evidence, even though spectral information can be critical for anomaly detection [17, 38].

To the best of our knowledge, in unsupervised TSAD, many methods emphasize either time-frequency modeling (e.g., [17]) or explicit multi-scale structure (e.g., [10]), while comparatively fewer works integrate both in a unified framework.

3 Method

Given a multivariate time-series window $X \in \mathbb{R}^{T \times C}$, the objective is to learn an unsupervised anomaly scoring function that outputs a timestamp-level anomaly map $\mathcal{A}(t)$.

3.1 Overview

As illustrated in Fig. 1, LEFT constructs three token streams: H^{time} , H^{freq} , and H^{ms} . It is based on a consistency premise: normal data maintain agreement across domains and resolutions, while anomalies violate it. Training is guided by multi-scale reconstruction, cycle consistency, cross-path consistency aligns the cycle pathway with the multi-scale pathway.

3.2 Tri-view Tokenization

3.2.1 Time Tokens. Time tokens provide a per-timestamp representation, which preserves local dynamics and abrupt deviations for timestamp-level scoring. We obtain them with a lightweight 1D convolutional stack $C_t^{(1d)}$ to provide a stable local inductive bias without resampling:

$$H^{\text{time}} = C_t^{(1d)}(X), \quad (1)$$

where $H^{\text{time}} \in \mathbb{R}^{T \times D}$ and the kernel sizes of $C_t^{(1d)}$ is $(5, 3, 1)$ that preserves temporal resolution T .

3.2.2 Frequency Tokens. Frequency tokens capture short-time spectral structure, including changes in periodicity and shifts in band-wise energy that may be hard to see in raw samples. We obtain S using a differentiable short-time Fourier transform W_θ . This design makes the frequency pathway directly trainable under the cycle consistency objective in Sec. 3.5, which encourages spectra that remain consistent with the reconstructed signal. The S is obtained via X :

$$S = W_\theta(X), \quad (2)$$

where $S \in \mathbb{R}^{C \times 2 \times F \times T_F}$, F is the number of frequency bins, and T_F is the number of STFT frames. Then a frequency encoder $C_f^{(2d)}$ produces frame-wise tokens:

$$H^{\text{freq}} = C_f^{(2d)}(S), \quad (3)$$

where $H^{\text{freq}} \in \mathbb{R}^{T_F \times D}$ and $C_f^{(2d)}$ treats $(2C)$ as channels, applies two 2D convolution layers with kernel size $(3, 3)$, pools over F to obtain frame-wise features, and projects to dimension D .

3.2.3 Multi-scale Structural Tokens via Nyquist-Constrained Learnable Filterbank. To capture multi-scale structure without fixed band partitions, we construct K band-limited downsampled sequences $\{\mathbf{X}^{(k)}\}_{k=1}^K$ using a Nyquist-constrained learnable filterbank. Unlike enlarging the receptive field, this construction explicitly produces cross-resolution structure, so coarse-to-fine agreement can be checked during training and inference. Multi-scale tokens are only useful if they remain stable after downsampling.

LEMMA 3.1. *The learned edges satisfy $0 = e_0 \leq e_1 \leq \dots \leq e_K$ and $e_k \leq c_k$ for all k . Define leakage beyond the cutoff by $\epsilon_k = \sum_{f > c_k} \tilde{m}_k(f)$.*

Let $\tilde{\mathbf{X}}^{(k)}(f) = \tilde{m}_k(f)\tilde{\mathbf{X}}(f)$, and $\mathbf{X}^{(k)} = \mathcal{D}_{r_k}(\mathcal{F}^{-1}(\tilde{\mathbf{X}}^{(k)}(f)))$. Then the aliasing energy after downsampling by r_k satisfies,

$$\begin{aligned} \|\Delta_{r_k}(\mathbf{X}^{(k)})\|_2 &\leq \vartheta(r_k) \|\tilde{\mathbf{X}}\|_2 \epsilon_k, \\ \epsilon_k &:= \sum_{f > c_k} \tilde{m}_k(f), \end{aligned} \quad (4)$$

where $\vartheta(r_k)$ depends only on r_k and FFT conventions.

Lemma 3.1 (proof in Appendix A.10) shows that a Nyquist-feasible learnable filterbank provides explicit control over aliasing. After downsampling, the aliasing energy is bounded by a term that scales with the out-of-cutoff leakage ϵ_k , so keeping ϵ_k small makes the downsampled component $\mathbf{X}^{(k)}$ a stable approximation of a band-limited signal. This property is important for uncovering normal and abnormal patterns in the multi-scale view. Under normal operation, most energy stays within the learned cutoff, so coarse tokens preserve consistent long-term structure and support reliable coarse-to-fine reconstruction. When abnormal behavior shifts energy across bands or introduces atypical high-frequency content, ϵ_k can increase and cross-scale agreement becomes harder to satisfy, which makes inconsistencies more detectable through reconstruction. Based on this result, we constrain each learned band by the Nyquist cutoff $c_k = \frac{1}{2r_k}$ so that $\mathbf{X}^{(k)}$ is obtained from a band-limited component. Residual coverage, together with the normalization in Eq. 8, further reduces the chance that large spectral regions are left effectively uncovered, preserving structural completeness even when band allocation is learned rather than fixed.

Given a boundary-extended signal $\tilde{\mathbf{X}}$, and its spectrum $\tilde{\mathbf{X}}(f)$ obtained by real FFT $\mathcal{F}(\tilde{\mathbf{X}})$, we apply K learnable soft masks $\{\tilde{m}_k(f)\}_{k=1}^K$:

$$\tilde{\mathbf{X}}^{(k)}(f) = \tilde{m}_k(f)\tilde{\mathbf{X}}(f), \quad k = 1, \dots, K. \quad (5)$$

Let downsampling factors $\{r_k\}_{k=1}^K$ be ordered coarse to fine ($r_1 \geq \dots \geq r_K$), and define normalized Nyquist cutoffs $c_k = \frac{1}{2r_k}$. Band edges are parameterized monotonically with learnable parameters $\{u_k\}$:

$$e_k = e_{k-1} + (c_k - e_{k-1})\sigma(u_k), \quad k = 1, \dots, K, \quad (6)$$

where $e_0 = 0$ and $\sigma(\cdot)$ is the logistic sigmoid. Given $s_\tau(x) = \sigma(x/(\tau + \varepsilon))$ with temperature $\tau > 0$, unnormalized band masks are constructed by:

$$m_k(f) = s_\tau(f - e_{k-1}) - s_\tau(f - e_k), \quad k = 1, \dots, K, \quad (7)$$

and normalized as:

$$\tilde{m}_k(f) = \frac{m_k(f)}{\sum_{j=1}^K m_j(f) + \varepsilon}. \quad (8)$$

so that they form a partition on the modeled structural band, i.e.,

$$\sum_{k=1}^K \tilde{m}_k(f) \approx 1 \quad \forall f \text{ s.t. } \sum_{k=1}^K m_k(f) > 0. \quad (9)$$

Each component is transformed back by inverse FFT and downsampled:

$$\mathbf{X}^{(k)} = \mathcal{D}_{r_k}(\mathcal{F}^{-1}(\tilde{\mathbf{X}}^{(k)}(f))), \quad T_k = \left\lceil \frac{T}{r_k} \right\rceil, \quad (10)$$

where $\mathbf{X}^{(k)} \in \mathbb{R}^{T_k \times C}$. Each scale is patch-tokenized and projected into D dimensions:

$$\mathbf{H}^{(k)} = \mathcal{P}(\mathbf{X}^{(k)}), \quad (11)$$

where $\mathbf{H}^{(k)} \in \mathbb{R}^{L_k \times D}$. To preserve scale-specific structural patterns within the multi-scale encoder, we use a scale independent attention mask $\mathbf{M}_{\text{blk}} \in \mathbb{R}^{L \times L}$ that is block-diagonal over scales and shared across layers. This prevents mixing across scales inside ϕ^{ms} . Cross-view and cross-resolution exchange is handled later by the tri-view interaction module:

$$\mathbf{H}^{\text{ms}} = \phi^{\text{ms}}\left(\text{Concat}(\mathbf{H}^{(1)}, \dots, \mathbf{H}^{(K)}); \mathbf{M}_{\text{blk}}\right), \quad (12)$$

where $\phi^{\text{ms}}(\cdot; \mathbf{M}_{\text{blk}})$ denotes a standard masked self-attention encoder.

3.3 Tri-view Interaction

Given $(\mathbf{H}^{\text{time}}, \mathbf{H}^{\text{freq}}, \mathbf{H}^{\text{ms}})$, LEFT uses lightweight token-level interaction to share evidence while preserving view-specific information. LEFT avoids dense all-pairs fusion because some view pairs are scale-mismatched. \mathbf{H}^{freq} is organized by STFT frames, while \mathbf{H}^{ms} comes from downsampled sequences. Direct attention between them would force implicit alignment across scales, which can overmix features and amplify noise.

LEFT therefore uses selected links. Time and frequency views are connected by the Fourier transform, so \mathbf{H}^{time} attends to \mathbf{H}^{freq} to inject spectral information into time-aligned representations, and \mathbf{H}^{freq} attends back to \mathbf{H}^{time} to stay tied to the raw signal. Multi-scale tokens are also derived from the time domain, so \mathbf{H}^{time} updates \mathbf{H}^{ms} . This design also allows frequency evidence to influence the multi-scale pathway indirectly through the updated time tokens \mathbf{H}^{time} . The **Fusion Strategy Analysis** further shows that all-pairs fusion or denser fusion does not improve performance in our setting.

The interaction module is a stack of L_f shared fusion blocks:

$$(\mathbf{H}^{\text{time+}}, \mathbf{H}^{\text{freq+}}, \mathbf{H}^{\text{ms+}}) = \Phi^{(L_f)}(\mathbf{H}^{\text{time}}, \mathbf{H}^{\text{freq}}, \mathbf{H}^{\text{ms}}), \quad (13)$$

where each $\Phi^{(L_f)}$ layer updates the three views via directed cross-attention: $\mathbf{H}^{\text{time}} = \phi^{\text{tf}(L_f)}(\mathbf{H}^{\text{time}}, \mathbf{H}^{\text{freq}})$, $\mathbf{H}^{\text{freq}} = \phi^{\text{ft}(L_f)}(\mathbf{H}^{\text{freq}}, \mathbf{H}^{\text{time}})$, and $\mathbf{H}^{\text{ms}} = \phi^{\text{mt}(L_f)}(\mathbf{H}^{\text{ms}}, \mathbf{H}^{\text{time}})$, followed by a token-wise residual with normalization. Finally, this selected fusion is closed by the cross-path constraint $\mathcal{L}_{\text{cons}}$ in Sec. 3.5, which ties the multi-scale reconstruction $\hat{\mathbf{X}}_{\text{ms}}$ to the cycle reconstruction $\hat{\mathbf{X}}_{\leftarrow f}$, so alignment learned through interaction is made verifiable at the reconstruction level rather than remaining a purely embedding-level agreement.

3.4 Prototype-based Time-Frequency Cycle Calibration and Memory Mixing

To provide a shared reference for matching time and frequency representations and reduce noisy or drifting alignment, we introduce two prototype banks $P_t, P_f \in \mathbb{R}^{M \times D}$ and map fused tokens to soft prototype assignments:

$$\mathbf{p}_t = \eta \left(\gamma \cos(\mathbf{H}^{\text{time+}}, P_t) \right), \quad \mathbf{p}_f = \eta \left(\gamma \cos(\mathbf{H}^{\text{freq+}}, P_f) \right), \quad (14)$$

where η is Softmax. $\cos(\cdot, \cdot)$ denotes cosine similarity and γ is a temperature. We align \mathbf{p}_f to length T by interpolation and define a bounded, symmetric inconsistency evidence via Jensen-Shannon (JS) divergence:

$$d(t) = \text{JS}(\mathbf{p}_t(t), \tilde{\mathbf{p}}_f(t)). \quad (15)$$

Lemma 3.3 gives a lower bound for this term. If the prototype assignments of the two views stay separated on an interval, the Jensen-Shannon discrepancy remains provably large on that interval.

We also derive an uncertainty gate $g(t)$ from assignment sharpness and entropy as an auxiliary scoring evidence.

The prototypes further act as a memory of stable patterns, read by time-averaged assignments:

$$\mathbf{z}_t^{\text{mem}} = (\text{Mean}_t(\mathbf{p}_t)) P_t, \quad \mathbf{z}_f^{\text{mem}} = (\text{Mean}_t(\mathbf{p}_f)) P_f. \quad (16)$$

Let $\mathbf{z}_t = \text{Mean}(\mathbf{H}^{\text{time+}})$ and $\mathbf{z}_f = \text{Mean}(\mathbf{H}^{\text{freq+}})$. We use curriculum memory mixing to stabilize decoding, gradually increasing the memory contribution with $\lambda \in [0, 1]$:

$$\mathbf{z}_t^+ = (1 - \lambda) \mathbf{z}_t + \lambda \mathbf{z}_t^{\text{mem}}, \quad \mathbf{z}_f^+ = (1 - \lambda) \mathbf{z}_f + \lambda \mathbf{z}_f^{\text{mem}}. \quad (17)$$

3.5 Time-Frequency Cycle Decoding

The time-frequency pathway is trained as a bidirectional closed loop through W_θ and W_θ^{-1} . The key purpose is to make the frequency prediction physically checkable: a valid $\hat{\mathbf{S}}$ should synthesize to a consistent signal, and a reconstructed signal should induce a consistent time-frequency representation. Without this loop, the frequency branch can be under-constrained and drift to spectra that match coarse energy statistics but are not synthesis-consistent, which weakens cross-domain discrepancy as an anomaly evidence.

We fuse time/frequency latents into a shared representation, $\mathbf{z} = \phi([\mathbf{z}_t^+; \mathbf{z}_f^+]) \in \mathbb{R}^D$. Then decode into both time and frequency outputs:

$$\hat{\mathbf{X}} = D_t(\mathbf{z}), \quad \hat{\mathbf{S}} = D_f(\mathbf{z}). \quad (18)$$

Define cycle reconstructions

$$\hat{\mathbf{X}}_{\leftarrow f} = W_\theta^{-1}(\hat{\mathbf{S}}), \quad \hat{\mathbf{S}}_{\rightarrow f} = W_\theta(\hat{\mathbf{X}}). \quad (19)$$

Enforcing both directions makes the two outputs mutually verifiable and discourages one-branch shortcut fitting: a spectrum is penalized if it cannot synthesize back to a consistent $\hat{\mathbf{X}}_{\leftarrow f}$, and a waveform is penalized if it induces an inconsistent $\hat{\mathbf{S}}_{\rightarrow f}$.

LEMMA 3.2. Suppose there exist constants $0 < A \leq B < \infty$ such that for any \mathbf{Y} for which $W_\theta(\mathbf{Y})$ is well-defined,

$$\sqrt{A} \|\mathbf{Y}\|_2 \leq \|W_\theta(\mathbf{Y})\|_2 \leq \sqrt{B} \|\mathbf{Y}\|_2. \quad (20)$$

Then the reconstruction errors in the time and time-frequency domains satisfy

$$\|\hat{\mathbf{X}} - \mathbf{X}\|_2 \leq \frac{1}{\sqrt{A}} \|\hat{\mathbf{S}}_{\rightarrow f} - \mathbf{S}\|_2, \quad (21)$$

$$\|\hat{\mathbf{S}}_{\rightarrow f} - \mathbf{S}\|_2 \leq \sqrt{B} \|\hat{\mathbf{X}} - \mathbf{X}\|_2, \quad (22)$$

where $\mathbf{S} = W_\theta(\mathbf{X})$ and $\hat{\mathbf{S}}_{\rightarrow f} = W_\theta(\hat{\mathbf{X}})$.

From Lemma 3.2 (proof is given in Appendix A.10), when the time-frequency transform W_θ satisfies frame bounds, the reconstruction errors in the time domain and the time-frequency domain bound each other up to constants. Therefore, beyond feature or score level fusion, we introduce the following cycle consistency constraint:

$$\mathcal{L}_{\text{cyc}} = l(\hat{\mathbf{S}}_{\rightarrow f}, \mathbf{S}) + l(\hat{\mathbf{X}}_{\leftarrow f}, \mathbf{X}). \quad (23)$$

We add a cross-path constraint to explicitly align the multi-scale reconstruction pathway with the time-frequency cycle pathway. This alignment is required for tri-view learning, since LEFT aims to enforce agreement among time, frequency, and multi-scale structure within a single model. The alignment target can be either $\hat{\mathbf{X}}_{\leftarrow f}$ or $\hat{\mathbf{X}}$. The cycle loss in Eq. 23 aligns both reconstructions to the same reference \mathbf{X} , and it also implies that $\hat{\mathbf{X}}_{\leftarrow f}$ and $\hat{\mathbf{X}}$ become close because $\|\hat{\mathbf{X}} - \hat{\mathbf{X}}_{\leftarrow f}\|_2 \leq \|\hat{\mathbf{X}} - \mathbf{X}\|_2 + \|\hat{\mathbf{X}}_{\leftarrow f} - \mathbf{X}\|_2$. Therefore, it is sufficient to constrain $\hat{\mathbf{X}}_{\text{ms}}$ to one of them. We choose $\hat{\mathbf{X}}_{\leftarrow f}$ and enforce their agreement by

$$\mathcal{L}_{\text{cons}} = l(\hat{\mathbf{X}}_{\text{ms}}, \hat{\mathbf{X}}_{\leftarrow f}). \quad (24)$$

This ties the multi-scale reconstruction pathway to the cycle pathway, so cross-resolution structure learned by $\hat{\mathbf{X}}_{\text{ms}}$ is required to agree with the synthesis-consistent reconstruction $\hat{\mathbf{X}}_{\leftarrow f}$. As a result, the tri-view alignment is enforced at the reconstruction level, and inconsistencies across-path become attributable to abnormal behavior rather than representation drift.

3.6 Multi-scale Reconstruction Head

The multi-scale pathway aims to reconstruct Nyquist-feasible structural content across resolutions, so that coarse-to-fine agreement can be explicitly checked. Starting from fused multi-scale tokens $\mathbf{H}^{\text{ms+}}$, we perform reconstruction in a coarse-to-fine manner: coarser tokens provide structural context while finer targets enforce detailed consistency. To retain scale-specific structure while injecting cross-view evidence, we combine the original multi-scale tokens and the interaction-enhanced tokens:

$$\tilde{\mathbf{H}}^{\text{ms}} = \beta_{\text{res}} \mathbf{H}^{\text{ms}} + \beta_{\text{inf}} \mathbf{H}^{\text{ms+}}, \quad (25)$$

where \mathbf{H}^{ms} preserves scale-pure structural evidence produced by the block-diagonal encoder in Eq. 12, while $\mathbf{H}^{\text{ms+}}$ carries alignment signals injected through tri-view interaction.

We then reconstruct multi-scale targets by splitting tokens by scale, upsampling in token space, and decoding patches:

$$\hat{\mathbf{Y}} = D_{\text{ms}}(\text{Up}(\text{Split}(\tilde{\mathbf{H}}^{\text{ms}}))), \quad (26)$$

which yields reconstructions for scales $k = 2, \dots, K$ and the full-rate reconstruction $\hat{\mathbf{X}}_{\text{ms}} \in \mathbb{R}^{T \times C}$. We treat the coarsest scale $k = 1$ as structural context and do not supervise it, since directly fitting

the coarsest component can encourage overly smooth solutions while contributing limited timestamp-level anomaly localization.

Define the multi-scale target:

$$Y = \text{Concat}(X^{(2)}, \dots, X^{(K)}, X). \quad (27)$$

We optimize a segment-aware objective so each scale contributes comparably despite different lengths:

$$\begin{aligned} \mathcal{L}_{\text{ms}} &= \sum_{k=2}^K \omega_k l(\hat{X}_{\text{ms}}^{(k)}, X^{(k)}) + \omega_{\text{full}} l(\hat{X}_{\text{ms}}, X), \\ \text{s.t. } & \sum_{k=2}^K \omega_k + \omega_{\text{full}} = 1, \end{aligned} \quad (28)$$

where $l(\cdot, \cdot)$ denotes SmoothL1.

3.7 Training Objective

LEFT is trained to make agreement an inherent property: the multi-scale pathway should reconstruct Nyquist-feasible structure across resolutions, the time-frequency pathway should satisfy bidirectional analysis-synthesis consistency, and the two pathways should agree on the full-rate reconstruction. Accordingly, the overall training loss combines (i) multi-scale reconstruction, (ii) cycle consistency, and (iii) cross-path consistency on the time domain:

$$\mathcal{L} = \lambda_{\text{ms}} \mathcal{L}_{\text{ms}} + \lambda_{\text{cyc}} \mathcal{L}_{\text{cyc}} + \lambda_{\text{cons}} \mathcal{L}_{\text{cons}}, \quad (29)$$

where \mathcal{L}_{ms} teaches scale-specific structure to be reconstructable, \mathcal{L}_{cyc} restricts the time-frequency outputs to be mutually reconstructable through W_θ and W_θ^{-1} , and $\mathcal{L}_{\text{cons}}$ locks the two pathways to a shared full-rate prediction, so discrepancies at inference can be attributed to abnormal behavior rather than pathway drift.

3.8 Tri-consistency Anomaly Scoring

At inference, LEFT scores anomalies as violations of agreement in two complementary forms: (i) inconsistency within the time-frequency cycle, and (ii) reconstruction residuals that across resolutions.

LEMMA 3.3. *Assume Lemma 3.2 holds. Assume further that the moving-average smoother MA_κ is a linear operator with nonnegative kernel weights $\{w_i\}$ satisfying $\sum_i w_i = 1$. Moreover, assume there exists a constant $\rho_\kappa \geq 1$ (depending only on κ and the boundary rule) such that for any nonnegative sequence $u(t)$,*

$$\left\langle (\text{MA}_\kappa(u))(t) \right\rangle_t \leq \rho_\kappa \langle u(t) \rangle_t. \quad (30)$$

Define the raw cycle magnitude inside the smoother by,

$$\tilde{\mathcal{A}}_{\text{cyc}}(t) = \alpha_f |\hat{X}_{\leftarrow f}(t) - X(t)| + \alpha_t |\hat{X}(t) - X(t)| + \alpha_g |g(t)| + \alpha_c c(t), \quad (31)$$

where $c(t) \geq 0$ is the cross-path discrepancy used in Eq. (36) (e.g., $c(t) = |\hat{X}_{\text{ms}}(t) - \hat{X}_{\leftarrow f}(t)|$). Recall that $\mathcal{A}_{\text{cyc}}(t) = (\text{MA}_\kappa(\tilde{\mathcal{A}}_{\text{cyc}}))(t)$ and $\mathcal{A}(t) = \alpha_{\text{cyc}} \mathcal{A}_{\text{cyc}}(t) + \alpha_{\text{ms}} \mathcal{A}_{\text{ms}}(t)$.

If training achieves $\mathcal{L}_{\text{ms}} \leq \varepsilon_{\text{ms}}$, $\mathcal{L}_{\text{cyc}} \leq \varepsilon_{\text{cyc}}$, and $\mathcal{L}_{\text{cons}} \leq \varepsilon_{\text{cons}}$, then the mean inference score satisfies,

$$\langle \mathcal{A}(t) \rangle_t \leq \kappa_{\text{ms}} \varepsilon_{\text{ms}} + \rho_\kappa \kappa_{\text{cyc}} \varepsilon_{\text{cyc}} + \rho_\kappa \kappa_{\text{cons}} \varepsilon_{\text{cons}} + \rho_\kappa \kappa_g \alpha_g \langle |g(t)| \rangle_t + \kappa_0, \quad (32)$$

where constants depend only on score aggregation weights, supervised scales, and ρ_κ .

Conversely, let $\Omega \subseteq \{1, \dots, T\}$ be a non-negligible subset. If

$\langle |\hat{X}(t) - X(t)| \rangle_{t \in \Omega} \geq \delta_t$, $\langle |\hat{X}_{\leftarrow f}(t) - X(t)| \rangle_{t \in \Omega} \geq \delta_f$, $\langle c(t) \rangle_{t \in \Omega} \geq \delta_c$, then the cycle component obeys,

$$\langle \tilde{\mathcal{A}}_{\text{cyc}}(t) \rangle_{t \in \Omega} \geq \alpha_t \delta_t + \alpha_f \delta_f + \alpha_c \delta_c. \quad (33)$$

If in addition the pointwise bounds $|\hat{X}(t) - X(t)| \geq \delta_t$, $|\hat{X}_{\leftarrow f}(t) - X(t)| \geq \delta_f$, and $c(t) \geq \delta_c$ hold for all $t \in \Omega$, then for any $t \in \Omega$ whose full averaging window of MA_κ lies inside Ω , one has $\mathcal{A}_{\text{cyc}}(t) \geq \alpha_t \delta_t + \alpha_f \delta_f + \alpha_c \delta_c$.

If additionally the prototype assignments satisfy $\|p_t(t) - \tilde{p}_f(t)\|_1 \geq \delta_p$ for all $t \in \Omega$, then the discrepancy evidence $d(t) = \text{JS}(p_t(t), \tilde{p}_f(t))$ obeys,

$$\langle d(t) \rangle_{t \in \Omega} \geq \frac{1}{8} \delta_p^2. \quad (34)$$

From Lemma 3.3 (proof is given in Appendix A.10), we propose a timestamp-level anomaly map:

$$\mathcal{A}(t) = \alpha_{\text{cyc}} \mathcal{A}_{\text{cyc}}(t) + \alpha_{\text{ms}} \mathcal{A}_{\text{ms}}(t), \quad (35)$$

where $\mathcal{A}_{\text{cyc}}(t)$ is the cycle-based discrepancy score and $\mathcal{A}_{\text{ms}}(t)$ is the multi-scale reconstruction score. We compute cycle residuals and apply a moving-average MA_κ with smoothing window size κ to suppress local noise and stabilize timestamp-level decisions:

$$\mathcal{A}_{\text{cyc}}(t) = \left(\text{MA}_\kappa(\alpha_f |\hat{X}_{\leftarrow f} - X| + \alpha_t |\hat{X} - X| + \alpha_g |g(t)| + \alpha_c c(t)) \right)(t), \quad (36)$$

where $c(t)$ measures cross-path discrepancy between the multi-scale pathway and the cycle pathway on the time domain, so disagreements penalized by $\mathcal{L}_{\text{cons}}$ during training can be directly reflected in the inference score.

The multi-scale score aggregates errors from all supervised scales by aligning them to the full resolution, so evidence that is salient at a coarse scale can still contribute to the fine-grained anomaly map:

$$\mathcal{A}_{\text{ms}}(t) = |\hat{X}_{\text{ms}}(t) - X(t)| + \sum_{k=2}^K \text{Up}_T(|\hat{X}_{\text{ms}}^{(k)} - X^{(k)}|)(t), \quad (37)$$

where $\text{Up}_T(\cdot)$ upsamples a sequence to length T . This design avoids relying on a single-view dominant residual: any-view irregularity can increase $\mathcal{A}(t)$ either through cycle disagreement, cross-path mismatch, or cross-resolution residual accumulation.

4 Experiments

4.1 Experimental Settings

Datasets. We evaluate LEFT on widely used TSAD benchmarks that cover server monitoring, space telemetry, and industrial control, including SMD [31], MSL [8], SMAP [8], SWaT [15], PSM [1], and GECCO [35] and SWAN [35] (see: Appendix A.1).

Baselines. We compare LEFT with 19 representative methods (see: Appendix A.2), covering both widely used classical approaches and recent SOTA neural models. Among these, *MtsCID*, *TimeMixer*, *TimesNet*, and *CrossAD* represent multi-scale SOTA methods that are closely related to our setting. Implementation details are provided in Appendix A.3.

Metrics. Evaluation in TSAD can be misleading under point adjustment, since even random predictors may obtain inflated scores [41, 42]. TSB-AD [12] further argues that *VUS-PR* [20] provides a more robust and less lag-sensitive evaluation, while several

Table 1: Results in the seven real-world datasets. The V-R and V-P are the VUS-ROC and VUS-PR, that higher indicate better performance. The best ones are in bold, and the second ones are underlined. \ddagger indicates statistical significance by t-test with $p < 0.05$. \dagger indicates statistical significance by t-test with $p < 0.1$.

Dataset Metric	SMD		MSL		SMAP		SWaT		PSM		GECCO		SWAN	
	V-R	V-P	V-R	V-P	V-R	V-P	V-R	V-P	V-R	V-P	V-R	V-P	V-R	V-P
OCSVM	0.6451	0.1131	0.5798	0.1753	0.4185	0.1133	0.5903	0.4396	0.5993	0.4252	0.7533	0.1207	0.9088	0.9004
PCA	0.7174	0.1529	0.6108	0.1889	0.4090	0.1144	0.6149	0.4459	0.6331	0.4706	0.5366	0.0443	0.9290	0.9123
IForest	0.7224	0.1304	0.5638	0.1631	0.4960	0.1315	0.3677	0.1011	0.6009	0.3964	0.7083	0.0943	0.8835	0.8793
LODA	0.6745	0.1213	0.5375	0.1689	0.3973	0.1017	0.6358	0.3531	0.6089	0.4423	0.5749	0.0339	0.9170	0.9107
HBOS	0.6670	0.1102	0.6265	0.1790	0.5620	0.1388	0.7084	0.4602	0.7056	0.5061	0.5440	0.0453	0.9056	0.8894
LOF	0.6893	0.1076	0.6081	0.1715	0.5673	0.1409	0.6667	0.4187	0.6628	0.4615	0.7817	0.0919	0.9095	0.9007
AE	0.7560	0.1542	0.6047	0.1890	0.4687	0.1366	0.5903	0.4144	0.6339	0.4490	0.6124	0.0448	0.6982	0.0201
DAGMM	0.6988	0.1496	0.6069	0.1803	0.5599	0.1349	0.5746	0.4731	0.5598	0.4522	0.5099	0.0396	0.8951	0.8697
LSTM	0.7001	0.1395	0.6163	0.1681	0.5329	0.1399	0.5482	0.2200	0.5571	0.4592	0.6450	0.0668	0.9082	0.8862
CAE	0.7174	0.1376	0.5382	0.1639	0.4212	0.1140	0.5939	0.4104	0.6113	0.4395	0.5524	0.0528	0.9042	0.9022
Omni	0.7080	0.1340	0.5490	0.1973	0.4743	0.1239	0.6187	0.4475	0.6340	0.4472	0.5386	0.0517	0.9041	0.9022
AT	0.5117	0.0796	0.3890	0.1041	0.4571	0.1239	0.5561	0.2679	0.5186	0.3309	0.4751	0.0278	0.8046	0.7943
DC	0.5145	0.0814	0.3900	0.0948	0.4444	0.1149	0.5191	0.1495	0.5235	0.3366	0.5454	0.0361	0.8429	0.8338
GPT4TS	0.7679	0.1745	0.7697	0.2769	0.5449	0.1289	0.2537	0.0846	0.6466	0.4599	0.9776	0.4181	0.9340	0.8924
ModernTCN	0.7707	0.1596	0.7747	0.3010	0.5470	0.1395	0.2735	0.0941	0.6480	0.4668	0.9694	0.4819	0.9027	0.8962
MtsCID	0.5162	0.0815	0.4686	0.1181	0.4260	0.1177	0.5021	0.1283	0.5194	0.3296	0.5315	0.0381	0.8128	0.8375
TimeMixer	0.7711	0.1391	0.7858	0.2461	0.5552	0.1371	0.2673	0.0918	0.5974	0.3807	0.9899	0.4606	0.9290	0.8721
TimesNet	0.8420	0.2040	0.7880	0.2731	0.5495	0.1352	0.2974	0.1158	0.6344	0.4373	0.9834	0.4578	0.9515	0.9160
CrossAD	0.8580	0.2344	0.8091	0.3144	0.5779	0.1443	0.7865	0.4767	0.7302	0.5596	0.9948	0.6211	0.9499	0.9171
LEFT	0.8638	0.2389	0.8157[‡]	0.3342[‡]	0.6562[‡]	0.1726[‡]	0.7991[‡]	0.5290[‡]	0.7836[‡]	0.5701[†]	0.9949[‡]	0.6634[‡]	0.9549[‡]	0.9244[‡]

common metrics can be biased across scenarios. We therefore report *VUS-PR* and *VUS-ROC* as the main metrics [20].

4.2 Detection Results

We evaluate LEFT on seven real-world TSAD benchmarks and compare it with 19 competitive baselines, as reported in Table 1. Across datasets with varied dynamics and anomaly types, LEFT achieves stronger ranking-based detection quality under both VUS-PR and VUS-ROC. LEFT improves both metrics on every benchmark relative to the strongest baseline in Table 1. Averaged over all datasets, LEFT improves by about 0.023 in VUS-ROC and 0.024 in VUS-PR over the best baseline (highlighted with underlining). Relative to the corresponding best-baseline averages (highlighted with underlining), this corresponds to improve about 3.50% in VUS-ROC and 6.90% in VUS-PR. The largest gains appear on SMAP, where LEFT improves VUS-ROC by 13.55% and VUS-PR by 19.61%, which matches the setting where cross-view and cross-scale evidence are especially important. Additional evaluation metrics are reported in Appendix A.4, where LEFT consistently outperforms the baselines.

4.3 Ablation Studies

As shown in Table 2, to evaluate the property of LEFT, we conduct detailed ablations. The results shows that LEFT achieves the best performance, which indicates that the gains come from the combined effect of the proposed modules rather than any single component. Removing tri-view interaction reduces the average from 0.7518 / 0.3590 to 0.7256 / 0.3455, showing that cross-view alignment contributes to detection quality. Replacing the learnable filterbank with a fixed one causes a similar average drop to 0.7261 / 0.3456 on average, suggesting that adaptive multi-scale structure captures evidence that fixed band splits miss in this setting. The largest effect comes from cycle consistency, since removing it

collapses average performance to 0.5422 / 0.2411, which supports the view that many anomalies are better exposed by agreement breaks between the time and frequency paths than by a dominant single-branch residual. Removing cross-path consistency lowers the average to 0.7266 / 0.3416, which is consistent with its role in aligning the multi-scale pathway with the time-frequency pathway. In Appendix A.5, we provide a more comprehensive ablation analysis by evaluating all combinations of the four key components.

4.4 Model Efficiency

We compare the efficiency of LEFT with representative TSAD methods on the PSM. The baselines cover several common design lines in recent work. AnomalyTransformer [41] uses a transformer and detects anomalies through association discrepancy. CrossAD [10] uses a transformer for multi-scale modeling. TimeMixer [34] uses MLP-based multi-scale mixing. TimesNet [37] uses frequency-aware convolutional modeling. All models are trained and tested on a single NVIDIA L40 GPU.

Table 3 shows that LEFT is the most efficient method across FLOPs, number of trainable parameters, and measured runtime. LEFT uses 188.849M FLOPs and 4.256M parameters. LEFT runs in 25.66 seconds per training epoch and 0.01527 seconds per 128 samples at inference. LEFT also shows clear efficiency advantages over strong baselines. The results suggest that LEFT stays small enough for typical deployment budgets, while its compute profile leads to clear wall-clock gains during both training and inference.

4.5 Model Analysis

4.5.1 Fusion Strategy Analysis. In this section, we compared with all-pairs fusion and two-view variants. In particular, all-pairs fusion, denoted as $M \leftrightarrow F \leftrightarrow T$, updates each view by aggregating information from the other two views, followed by residual addition and

Table 2: Ablation studies for LEFT. The V-R and V-P are the VUS-ROC and VUS-PR, that higher indicate better performance. The best ones are in bold. ‘↓’ marks a severe (over 5%) performance drop compared with the best results. Full results are listed in Appendix A.5.

Architecture	PSM		MSL		SMAP	
	V-R	V-P	V-R	V-P	V-R	V-P
w/o Tri-view Interaction	0.7814	0.5653	0.8142	0.3235	0.5814↓	0.1477↓
w/o Learnable Filterbank	0.7748	0.5564	0.8082	0.3254	0.5952↓	0.1549↓
w/o Cycle Consistency	0.6497↓	0.4407↓	0.5283↓	0.1666↓	0.4487↓	0.1161↓
w/o Cross-path Consistency	0.7753	0.5516	0.8100	0.3251	0.5946↓	0.1480↓
LEFT	0.7836	0.5701	0.8157	0.3342	0.6562	0.1726

Table 3: Comparison of various methods w.r.t FLOPs, # params, training time, inference time. # params represents the total number of trainable parameters of the model. Training time represents the time cost to train the model for each epoch with batch size 128, while inference time indicates the duration required to process 128 samples.

Method	FLOPs	# Params	Training Time (s)	Inference Time (s)
TimesNet	21.145 G	36.734 M	285.80	0.10372
TimeMixer	11.967 G	1.349 M	630.19	0.28682
AnomalyTransformer	920.912 M	4.799 M	59.86	0.03076
CrossAD	1.288 G	927.750 K	205.22	0.06712
LEFT	188.849 M	4.256 M	25.66	0.01527

layer normalization. The two-view variants $M \leftrightarrow F$, $M \leftrightarrow T$, and $T \leftrightarrow F$ enable interaction only within the selected pair of views, while keeping the third view unchanged. In particular, $T \leftrightarrow F$ exchanges information only between time and frequency tokens, $M \leftrightarrow T$ exchanges information only between multi-scale and time tokens, and $M \leftrightarrow F$ exchanges information only between multi-scale and frequency tokens. The impact of different fusion strategies on detection performance is reported in Table 4. Across PSM, MSL, and SMAP, the proposed tri-view fusion yields the competitive overall performance. It consistently improves over the best two-view variant in both VUS-ROC and VUS-PR, showing that using all three evidence jointly is more effective than relying on any pair of views. All-pairs fusion is not always better. It adds many cross-view links, which can mix the views too strongly and spread noise across branches. This can weaken discrepancy signals and hurt performance on some datasets. In contrast, the proposed fusion uses a selected set of interactions, which is enough to align the views, but it keeps view-specific information separated so discrepancies stay meaningful for anomaly scoring. In Appendix A.6, we provide a more comprehensive ablation analysis of fusion strategies.

4.5.2 λ_{cyc} and λ_{cons} Sensitivity. Figs. 2 (a) and (b) suggest that detection quality depends on the joint choice of cycle consistency and cross-path consistency. LEFT remains competitive when cycle consistency is strong and cross-path consistency is relatively weak. Pushing cross-path consistency to large values does not yield stable gains. The results suggest that an overly strong cross-path consistency weight can over-align the pathways and weaken fault

Table 4: Fusion strategy ablation. V-R and V-P are the VUS-ROC and VUS-PR. The best ones are in bold. ‘↓’ marks a severe (over 5%) performance drop compared with the best results.

Fusion Method	PSM		MSL		SMAP	
	V-R	V-P	V-R	V-P	V-R	V-P
$M \leftrightarrow F \leftrightarrow T$	0.7860	0.5692	0.8106	0.3246	0.4776↓	0.1295↓
$M \leftrightarrow F$	0.7687	0.5479	0.8069	0.3255	0.5640↓	0.1419↓
$M \leftrightarrow T$	0.7558	0.5371	0.8051	0.3149	0.4330↓	0.1163↓
$T \leftrightarrow F$	0.7790	0.5593	0.8121	0.3265	0.6203↓	0.1634↓
Default	0.7836	0.5701	0.8157	0.3342	0.6562	0.1726

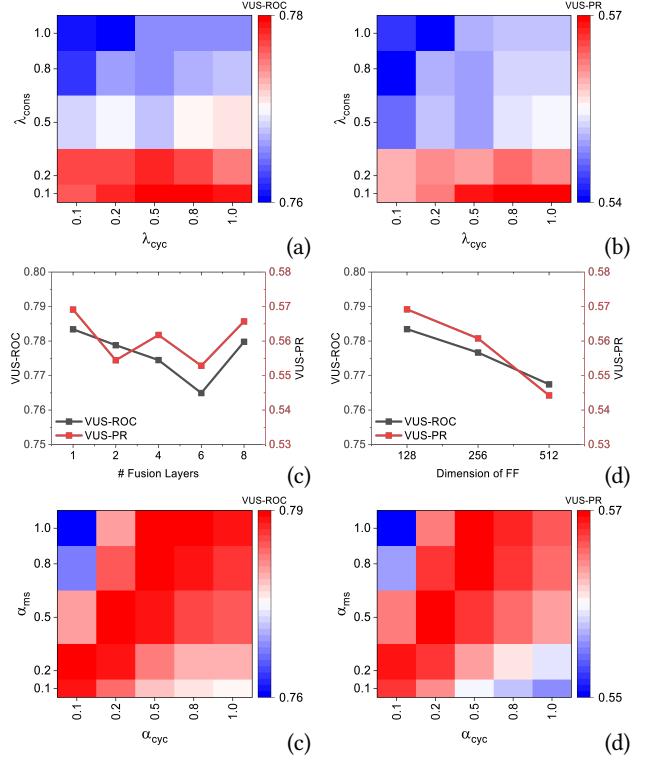


Figure 2: Fusion hyper-parameters sensitivity analysis on the PSM dataset. (a) and (b) show the sensitivity to λ_{cyc} and λ_{cons} . (c) and (d) present the depth and width analysis. (e) and (f): α_{cyc} and α_{ms} sensitivity. More results are listed in Appendix A.7.

evidence. A stronger cycle consistency weight is often beneficial because it better exploits the natural analysis-synthesis link between time and frequency views.

4.5.3 Fusion Hyper-parameters Analysis. Figs. 2 (c) and (d) show that increasing the depth or width of the fusion layer does not produce a meaningful performance gain, which aligns with the observation in Sec. 4.5.1 that stronger fusion is not always better. In this setting, a heavier fusion tends to over-mix the views, so distinctive evidence become less separable in the shared representation.

4.5.4 α_{cyc} and α_{ms} Sensitivity. Figs. 2 (e) and (f) show that both VUS-ROC and VUS-PR depend on the joint choice of α_{cyc} and α_{ms} ,

and neither metric improves monotonically when only one weight is increased. High-score regions concentrate in a middle range of the grid, while several extreme settings lead to lower values. This pattern echoes our main contribution that LEFT gains from combining cycle disagreement and reconstruction disagreement with multi-scale residual evidence, where reliable detection comes from their complementary use rather than amplifying a single term.

5 Conclusion

We propose LEFT, a unified tri-view framework for unsupervised TSAD. LEFT constructs time tokens, frequency tokens from a differentiable STFT, and multi-scale structural tokens from a Nyquist-constrained learnable filterbank with residual coverage. LEFT uses lightweight token interactions to fuse the three views and expose cross-view inconsistency. It also applies cross-scale reconstruction consistency and time-frequency cycle consistency, which makes the inconsistency signal more reliable. Experiments on real-world benchmarks show that LEFT improves both accuracy and efficiency. Compared with strong baselines, LEFT improves VUS-ROC and VUS-PR by about 3% and 6%, respectively and reduces FLOPs by over 80%, speeds up training by about 8 \times . Future work will study when cross-view inconsistency is most informative and will improve interpretability by linking detected anomalies to specific time-frequency or cross-scale conflicts.

References

- [1] Ahmed Abdulaal, Zhuanghua Liu, and Tomer Lancewicki. 2021. Practical Approach to Asynchronous Multivariate Time Series Anomaly Detection and Localization. In *Proceedings of the 27th ACM SIGKDD Conference on Knowledge Discovery & Data Mining*. 2485–2494.
- [2] Ali Behrouz, Michele Santacatterina, and Ramin Zabih. 2024. Chimera: Effectively modeling multivariate time series with 2-dimensional state space models. *Advances in Neural Information Processing Systems* 37 (2024), 119886–119918.
- [3] Markus M. Breunig, Hans-Peter Kriegel, Raymond T. Ng, and Jörg Sander. 2000. LOF: identifying density-based local outliers. In *Proceedings of the 2000 ACM SIGMOD International Conference on Management of Data*. 93–104.
- [4] David Campos, Tung Kieu, Chenjuan Guo, Feiteng Huang, Kai Zheng, Bin Yang, and Christian S. Jensen. 2021. Unsupervised time series outlier detection with diversity-driven convolutional ensembles. *Proceedings of the VLDB* 15, 3 (Nov. 2021), 611–623.
- [5] Zhaoliang Chen, Zhihao Wu, William K. Cheung, Hong-Ning Dai, Byron Choi, and Jiming Liu. 2025. MSHTrans: Multi-Scale Hypergraph Transformer with Time-Series Decomposition for Temporal Anomaly Detection. In *Proceedings of the 31st ACM SIGKDD Conference on Knowledge Discovery and Data Mining* V.2. 274–285.
- [6] Yuchen Fang, Jiandong Xie, Yan Zhao, Lu Chen, Yunjun Gao, and Kai Zheng. 2024. Temporal-frequency masked autoencoders for time series anomaly detection. In *2024 IEEE 40th International Conference on Data Engineering (ICDE)*. 1228–1241.
- [7] Markus Goldstein and Andreas Dengel. 2012. Histogram-based outlier score (hbos): A fast unsupervised anomaly detection algorithm. *KI-2012: Poster and Demo Track* 1 (2012), 59–63.
- [8] Kyle Hundman, Valentino Constantinou, Christopher Laporte, Ian Colwell, and Tom Soderstrom. 2018. Detecting Spacecraft Anomalies Using LSTMs and Non-parametric Dynamic Thresholding. In *Proceedings of the 24th ACM SIGKDD International Conference on Knowledge Discovery & Data Mining*. 387–395.
- [9] Ming Jin, Huan Yee Koh, Qingsong Wen, Daniele Zambon, Cesare Alippi, Geoffrey I. Webb, Irwin King, and Shirui Pan. 2024. A survey on graph neural networks for time series: Forecasting, classification, imputation, and anomaly detection. *IEEE Transactions on Pattern Analysis and Machine Intelligence* (2024).
- [10] Beibei Li, Qichao Shentu, Yang Shu, Hui Zhang, Ming Li, Ning Jin, Bin Yang, and Chenjuan Guo. 2025. CrossAD: Time Series Anomaly Detection with Cross-scale Associations and Cross-window Modeling. In *The Thirty-ninth Annual Conference on Neural Information Processing Systems*.
- [11] Fei Tony Liu, Kai Ming Ting, and Zhi-Hua Zhou. 2008. Isolation Forest. In *The Eighth IEEE International Conference on Data Mining*.
- [12] Qinghua Liu and John Paparrizos. 2024. The elephant in the room: Towards a reliable time-series anomaly detection benchmark. *Advances in Neural Information Processing Systems* 37 (2024), 108231–108261.
- [13] Donghao Luo and Xue Wang. 2024. ModernTCN: A modern pure convolution structure for general time series analysis. In *The twelfth International Conference on Learning Representations*. 1–43.
- [14] Jiaming Ma, Binwu Wang, Qihe Huang, Guanjun Wang, Pengkun Wang, Zhengyang Zhou, and Yang Wang. 2025. Mofo: Empowering long-term time series forecasting with periodic pattern modeling. In *The Thirty-ninth Annual Conference on Neural Information Processing Systems*.
- [15] Aditya P. Mathur and Nils Ole Tippenhauer. 2016. SWaT: A water treatment testbed for research and training on ICS security. In *2016 International Workshop on Cyber-physical Systems for Smart Water Networks (CySWater)*. 31–36.
- [16] SHYU Mei-Ling. 2003. A Novel Anomaly Detection Scheme Based on Principal Component Classifier. In *Proc. of ICDM Foundation and New Direction of Data Mining*.
- [17] Youngeun Nam, Susik Yoon, Yooju Shin, Minyoung Bae, Hwanjun Song, Jae-Gil Lee, and Byung Suk Lee. 2024. Breaking the Time-Frequency Granularity Discrepancy in Time-Series Anomaly Detection. In *Proceedings of the ACM Web Conference 2024*. 4204–4215.
- [18] Yuqi Nie, Nam H. Nguyen, Phanwadee Sinthong, and Jayant Kalagnanam. 2022. A Time Series is Worth 64 Words: Long-term Forecasting with Transformers. In *The Eleventh International Conference on Learning Representations*.
- [19] John Paparrizos, Paul Boniol, Qinghua Liu, and Themis Palpanas. 2025. Advances in Time-Series Anomaly Detection: Algorithms, Benchmarks, and Evaluation Measures. In *Proceedings of the 31st ACM SIGKDD Conference on Knowledge Discovery and Data Mining* V.2. 6151–6161.
- [20] John Paparrizos, Paul Boniol, Themis Palpanas, Ruey S. Tsay, Aaron Elmore, and Michael J. Franklin. 2022. Volume under the surface: a new accuracy evaluation measure for time-series anomaly detection. *Proceedings of the VLDB* 15, 11 (July 2022), 2774–2787.
- [21] Tomáš Pevný. 2016. Loda: Lightweight on-line detector of anomalies. *Machine Learning* 102, 2 (Feb. 2016), 275–304.
- [22] Xiangfei Qiu, Jilin Hu, Lekui Zhou, Xingjian Wu, Junyang Du, Buang Zhang, Chenjuan Guo, Aoying Zhou, Christian S. Jensen, Zhenli Sheng, and Bin Yang. 2024. TFB: Towards Comprehensive and Fair Benchmarking of Time Series Forecasting Methods. *Proceedings of the VLDB Endowment* 17, 9 (May 2024), 2363–2377.
- [23] Xiangfei Qiu, Zhe Li, Wanghui Qiu, Shiyuan Hu, Lekui Zhou, Xingjian Wu, Zhengyu Li, Chenjuan Guo, Aoying Zhou, Zhenli Sheng, Jilin Hu, Christian S. Jensen, and Bin Yang. 2025. TAB: Unified Benchmarking of Time Series Anomaly Detection Methods. <http://arxiv.org/abs/2506.18046> [cs].
- [24] Mayu Sakurada and Takehisa Yairi. 2014. Anomaly Detection Using Autoencoders with Nonlinear Dimensionality Reduction. In *Proceedings of the MLSDA 2014 2nd Workshop on Machine Learning for Sensory Data Analysis*. 4–11.
- [25] Sebastian Schmid, Felix Naumann, and Thorsten Papenbrock. 2024. AutoTSAD: Unsupervised Holistic Anomaly Detection for Time Series Data. *Proceedings of the VLDB Endowment* 17, 11 (July 2024), 2987–3002.
- [26] Bernhard Schölkopf, Robert C. Williamson, Alex Smola, John Shawe-Taylor, and John Platt. 1999. Support vector method for novelty detection. *Advances in Neural Information Processing Systems* 12 (1999).
- [27] Lifeng Shen, Zhongzhong Yu, Qianli Ma, and James T. Kwok. 2021. Time series anomaly detection with multiresolution ensemble decoding. In *Proceedings of the AAAI Conference on Artificial Intelligence*, Vol. 35. 9567–9575.
- [28] Qichao Shentu, Beibei Li, Kai Zhao, Yang Shu, Zhongwen Rao, Lujia Pan, Bin Yang, and Chenjuan Guo. 2024. Towards a General Time Series Anomaly Detector with Adaptive Bottlenecks and Dual Adversarial Decoders. In *The Thirteenth International Conference on Learning Representations*.
- [29] Alban Siffer, Pierre-Alain Fouque, Alexandre Termier, and Christine Largouet. 2017. Anomaly Detection in Streams with Extreme Value Theory. In *Proceedings of the 23rd ACM SIGKDD International Conference on Knowledge Discovery and Data Mining*. 1067–1075.
- [30] Junho Song, Keonwoo Kim, Jeonglyul Oh, and Sungjoon Cho. 2023. Memto: Memory-guided transformer for multivariate time series anomaly detection. *Advances in Neural Information Processing Systems* 36 (2023), 57947–57963.
- [31] Ya Su, Youjian Zhao, Chenhao Niu, Rong Liu, Wei Sun, and Dan Pei. 2019. Robust Anomaly Detection for Multivariate Time Series through Stochastic Recurrent Neural Network. In *Proceedings of the 25th ACM SIGKDD International Conference on Knowledge Discovery & Data Mining*. 2828–2837.
- [32] David M.J. Tax and Robert P.W. Duin. 2004. Support Vector Data Description. *Machine Learning* 54, 1 (Jan. 2004), 45–66.
- [33] Chengsen Wang, Zirui Zhuang, Qi Qi, Jingyu Wang, Xingyu Wang, Haifeng Sun, and Jianxin Liao. 2023. Drift doesn't matter: Dynamic decomposition with diffusion reconstruction for unstable multivariate time series anomaly detection. *Advances in Neural Information Processing Systems* 36 (2023), 10758–10774.
- [34] Shiyu Wang, Haixu Wu, Xiaoming Shi, Tengge Hu, Huakun Luo, Lintao Ma, James Y. Zhang, and JUN ZHOU. 2024. TimeMixer: Decomposable Multiscale Mixing for Time Series Forecasting. In *The Twelfth International Conference on Learning Representations*.
- [35] Zexin Wang, Changhua Pei, Minghua Ma, Xin Wang, Zhihan Li, Dan Pei, Saravanan Rajmohan, Dongmei Zhang, Qingwei Lin, Haiming Zhang, Jianhui Li, and

Gaogang Xie. 2024. Revisiting VAE for Unsupervised Time Series Anomaly Detection: A Frequency Perspective. In *Proceedings of the ACM Web Conference 2024*. 3096–3105.

[36] Scott Wisdom, John R. Hershey, Kevin Wilson, Jeremy Thorpe, Michael Chinien, Brian Patton, and Rif A. Saurous. 2019. Differentiable consistency constraints for improved deep speech enhancement. In *ICASSP 2019-2019 IEEE International Conference on Acoustics, Speech and Signal Processing (ICASSP)*. 900–904.

[37] Haixu Wu, Tengge Hu, Yong Liu, Hang Zhou, Jianmin Wang, and Mingsheng Long. 2022. TimesNet: Temporal 2D-Variation Modeling for General Time Series Analysis. In *The Eleventh International Conference on Learning Representations*.

[38] Xingjian Wu, Xiangfei Qiu, Zhengyu Li, Yihang Wang, Jinlin Hu, Chenjuan Guo, Hui Xiong, and Bin Yang. 2024. CATCH: Channel-Aware Multivariate Time Series Anomaly Detection via Frequency Patching. In *The Thirteenth International Conference on Learning Representations*.

[39] Mingyu Xia, Chunxu Zhang, Zijian Zhang, Hao Miao, Qidong Liu, Yuanshao Zhu, and Bo Yang. [n. d.]. TimeEmb: A Lightweight Static-Dynamic Disentanglement Framework for Time Series Forecasting. In *The Thirty-ninth Annual Conference on Neural Information Processing Systems*.

[40] Yongzheng Xie, Hongyu Zhang, and Muhammad Ali Babar. 2025. Multivariate Time Series Anomaly Detection by Capturing Coarse-Grained Intra- and Inter-Variate Dependencies. In *Proceedings of the ACM on Web Conference 2025*. 697–705.

[41] Jiehui Xu, Haixu Wu, Jianmin Wang, and Mingsheng Long. 2021. Anomaly Transformer: Time Series Anomaly Detection with Association Discrepancy. In *International Conference on Learning Representations*.

[42] Yiyuan Yang, Chaoli Zhang, Tian Zhou, Qingsong Wen, and Liang Sun. 2023. DCdetector: Dual Attention Contrastive Representation Learning for Time Series Anomaly Detection. In *Proceedings of the 29th ACM SIGKDD Conference on Knowledge Discovery and Data Mining*. 3033–3045.

[43] Tianyi Yin, Jingwei Wang, Yunlong Ma, Han Wang, Chenze Wang, Yukai Zhao, Min Liu, and Weiming Shen. 2025. Apollo-Forecast: Overcoming Aliasing and Inference Speed Challenges in Language Models for Time Series Forecasting. In *Proceedings of the AAAI Conference on Artificial Intelligence*, Vol. 39. 22173–22181. Issue: 21.

[44] Chuxu Zhang, Dongjin Song, Yuncong Chen, Xinyang Feng, Cristian Lumezanu, Wei Cheng, Jingchao Ni, Bo Zong, Haifeng Chen, and Nitesh V. Chawla. 2019. A deep neural network for unsupervised anomaly detection and diagnosis in multivariate time series data. In *Proceedings of the AAAI Conference on Artificial Intelligence*, Vol. 33. 1409–1416.

[45] Yahao Zhang, Xiaofeng Zhou, Yichi Zhang, Shuai Li, and Shurui Liu. 2025. Improving time series forecasting in frequency domain using a multi resolution dual branch mixer with noise insensitive ArcTanLoss. *Scientific Reports* 15, 1 (2025), 12557.

[46] Guojin Zhong, Jin Yuan, Zhiyong Li, and Long Chen. 2025. Multi-resolution decomposable diffusion model for non-stationary time series anomaly detection. In *The Thirteenth International Conference on Learning Representations*.

[47] Tian Zhou, Ziqing Ma, Qingsong Wen, Xue Wang, Liang Sun, and Rong Jin. 2022. Fedformer: Frequency enhanced decomposed transformer for long-term series forecasting. In *International Conference on Machine Learning*. 27268–27286.

[48] Tian Zhou, Peisong Niu, Liang Sun, and Rong Jin. 2023. One fits all: Power general time series analysis by pretrained lm. *Advances in Neural Information Processing Systems* 36 (2023), 43322–43355.

[49] Bo Zong, Qi Song, Martin Renqiang Min, Wei Cheng, Cristian Lumezanu, Daeki Cho, and Haifeng Chen. 2018. Deep autoencoding gaussian mixture model for unsupervised anomaly detection. In *International Conference on Learning Representations*.

Appendix

A.1 Datasets

To evaluate LEFT, we conduct experiments on multiple public TSAD benchmarks. We evaluate LEFT on benchmark datasets from server monitoring, space telemetry, and industrial control. *SMD* contains resource-utilization measurements from server machines [31]. *MSL* and *SMAP* are NASA telemetry datasets with multivariate sensor and actuator signals [8]. *SWaT* records sensor traces from a water-treatment testbed under normal operation and attack scenarios [15]. *PSM* provides performance metrics collected from eBay server machines [1]. We also use *NeurIPS-TS* (NeurIPS 2021 Time Series Benchmark) and report results on its *GECCO* and *SWAN* subsets [35].

For *MSL* and *SMAP*, we follow prior work [10, 28, 33] and keep only the first continuous channel, since discrete variables are not well suited to reconstruction-based scoring.

Dataset details are provided in Table A1. We follow [10] for the data split and sliding-window setup.

Table A1: Dataset statistics. AR (anomaly ratio) denotes the fraction of anomalous points in each dataset.

Dataset	Domain	Dimension	Window	Training	Validation	Test (labeled)	AR (%)
MSL	Spacecraft	1	96	46,653	11,664	73,729	10.5
PSM	Server Machine	25	192	105,984	26,497	87,841	27.8
SMAP	Spacecraft	1	192	108,146	27,037	427,617	12.8
SMD	Server Machine	38	192	566,724	141,681	708,420	4.2
SWaT	Water treatment	31	192	396,000	99,000	449,919	12.1
GECCO	Water treatment	9	128	55,408	13,852	69,261	1.25
SWAN	Space Weather	38	192	48,000	12,000	60,000	23.8

A.2 Baselines

The baselines include linear transformation-based methods, such as *OCSVM*[26] and *PCA*[16], as well as outlier-oriented detectors, including *IForest*[11] and *LODA*[21]. We further consider density-based methods (*HBOS*[7], *LOF*[3]), which remain competitive on low-dimensional regimes but can be sensitive to complex temporal drift. Neural baselines span reconstruction and forecasting families, including *AutoEncoder* (AE)[24], *DAGMM*[49], *LSTM*[8], *CAE-Ensemble* (CAE)[4], and *Omni-Anomaly* (Omni)[31]. We also include recent transformer- and contrastive-based TSAD models, such as *Anomaly Transformer* (AT)[41], *DCdetector* (DC)[42], *ModernTCN*[13], *GPT4TS*[48], *MtsCID*[40], *TimeMixer*[34], and *TimesNet*[37], together with *CrossAD*[10]. Among these, *MtsCID*, *TimeMixer*, *TimesNet*, and *CrossAD* represent multi-scale SOTA methods that are closely related to our setting.

A.3 Implement Details

In our setup, the time-view encoder is a lightweight 1D convolutional stack with kernel sizes (5, 3, 1), while the frequency-view encoder is a lightweight 2D convolutional stack with two (3, 3) layers. All decoders are two-layer MLPs. We use sliding windows for both training and inference, and report results under a non-overlapping window protocol. Dataset-specific window lengths are given in Table A1. Optimization uses Adam with learning rate 10^{-4} and batch size 128. Following [22], we keep all test windows at inference time and do not apply the drop-last trick. We set decision thresholds with SPOT [29], consistent with prior TSAD practice [10, 28]. All experiments are implemented in PyTorch and run on a single NVIDIA L40 GPU. More details are available at <https://anonymous.4open.science/r/Left-6366>.

A.4 Multi-metric Results

For a comprehensive comparison, we report additional evaluation metrics in Table A2. We include AUC-ROC (AUC-R), AUC-PR (AUC-P), Range-AUC-ROC (R-A-R), Range-AUC-PR (R-A-P), Accuracy (Acc), and Standard F1 (F1). Here we compare only with *CrossAD* [10], since it is the best-performing baseline in our main results (see Table 1). The results show that LEFT performs strongly across these metrics, which further supports its effectiveness for time series anomaly detection.

Table A2: Multi-metrics results in the three real-world datasets. The higher values for all metrics represent better performance. The best ones are in bold.

Dataset	Model	AUC-R	AUC-P	R-A-R	R-A-P	ACC	F1
PSM	CrossAD	0.6523	0.4706	0.7292	0.5733	0.6274	0.4675
	LEFT	0.7755	0.5753	0.7858	0.5890	0.6555	0.5693
MSL	CrossAD	0.7808	0.2837	0.8095	0.3409	0.6786	0.3361
	LEFT	0.7878	0.3019	0.8121	0.3546	0.7296	0.3436
SMAP	CrossAD	0.5577	0.1333	0.5926	0.1527	0.4285	0.2792
	LEFT	0.6411	0.1618	0.6667	0.1821	0.5842	0.3053

A.5 Ablation Study Details

This appendix reports the full ablation results as shown in Table A3, including variants where each component is removed individually.

The results show that the LEFT achieves the best performance on each dataset and on average, reaching 0.7518 in VUS-ROC and 0.3590 in VUS-PR, which indicates that the strongest results arise when the components are used together. Among single-component variants, cycle consistency yields the most pronounced improvement, with the cycle-only setting in Row 3 improving the average to 0.6880 / 0.3320, whereas the other single-component settings remain close to the low baseline range. The importance of cycle consistency is further confirmed by Row 13, where removing it while keeping the other three components causes a sharp drop to 0.5422 / 0.2411. When cycle consistency is present, adding tri-view interaction or the learnable filterbank produces clear additional gains, as shown by Row 9 and Row 7 compared with Row 3, and the three-component configurations in Rows 11 and 12 remain notably below the full model. Cross-path consistency also contributes beyond the cycle constraint, as removing it in Row 14 reduces the average from 0.7518 / 0.3590 to 0.7266 / 0.3416. Overall, the ablations support that enforcing time-frequency agreement is central for reliable learning, while the remaining components further improve performance when integrated into the same training and scoring framework.

A.6 Fusion Strategy Ablation

Table A4 compares several fusion strategies on PSM, MSL, and SMAP using VUS-ROC, VUS-PR, and measured training and inference time. The proposed strategy provides the most consistent detection quality across datasets. It achieves the best VUS-PR on PSM and the best VUS-ROC and VUS-PR on both MSL and SMAP. All-pairs fusion $M \leftrightarrow F \leftrightarrow T$ attains the highest VUS-ROC on PSM, yet it incurs higher compute cost and its scores drop markedly on SMAP, showing that denser interaction does not yield stable gains across settings. The two-view ablations offer additional context. The $T \leftrightarrow F$ variant remains competitive on PSM and MSL, and it clearly outperforms $M \leftrightarrow F$ and $M \leftrightarrow T$ on SMAP, which suggests that direct time-frequency exchange is an important interaction path in this table. In contrast, strategies that rely on mixing M with a single branch show weaker ranking quality, even though their runtimes are similar to proposed.

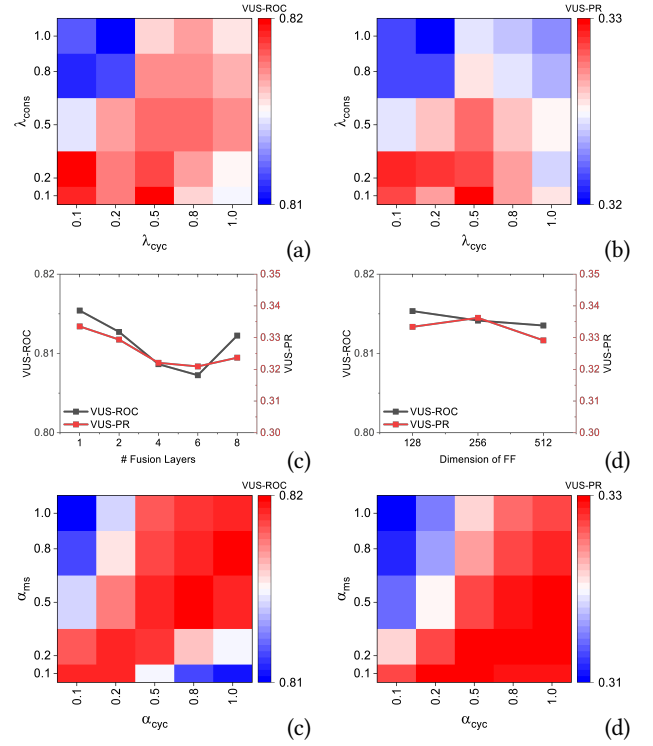


Figure A1: Fusion hyper-parameters sensitivity analysis on the MSL dataset. (a) and (b) show the sensitivity to λ_{cyc} and λ_{cons} . (c) and (d) present the depth and width analysis. (e) and (f): α_{cyc} and α_{ms} sensitivity.

A.7 Fusion Hyper-parameters Sensitivity

The Figs. A1 and A2 support the claim that performance is driven by the joint setting of cycle consistency and cross path consistency. In Figs. A1(a,b) and A2(a,b), the optimal cluster where cross-path consistency stays low while cycle consistency is kept at a moderate level, and pushing cross-path consistency toward large values does not yield reliable improvements. Figs. A1(c,d) and A2(c,d) further show that increasing fusion depth or width brings no meaningful gain, and several settings slightly reduce VUS-ROC or VUS-PR, which is consistent with the observation that stronger fusion is not automatically beneficial in this setup. Figs. A1(e,f) and A2(e,f) further show that both VUS-ROC and VUS-PR vary with the joint choice of α_{cyc} and α_{ms} . The trend is not monotonic along either axis, since increasing one weight does not reliably improve the score when the other is fixed. Higher values concentrate in a middle region of the grid, where α_{cyc} is moderate to large and α_{ms} stays away from its maximum, while several boundary settings yield lower scores. The same pattern appears in both metrics, which aligns with our scoring design that balances cycle-based disagreement and multi-scale residual evidence rather than letting one term dominate.

Table A3: Ablation studies details for LEFT. The V-R and V-P are the VUS-ROC and VUS-PR, that higher indicate better performance. The best ones are in bold. The learnable filterbank indicates whether the filterbank is learnable (✓) or fixed (✗).

	Dataset				PSM		MSL		SMAP		avg.	
	Tri-view Interaction	Learnable Filterbank	Cycle Consistency	Cross-path Consistency	V-R	V-P	V-R	V-P	V-R	V-P	V-R	V-P
1	✓	✗	✗	✗	0.6513	0.4438	0.5495	0.1849	0.4212	0.1138	0.5407	0.2475
2	✗	✓	✗	✗	0.6523	0.4447	0.5584	0.1869	0.4586	0.1202	0.5564	0.2506
3	✗	✗	✓	✗	0.7748	0.5491	0.7616	0.3090	0.5277	0.1378	0.6880	0.3320
4	✗	✗	✗	✓	0.6497	0.4415	0.5226	0.1572	0.4727	0.1269	0.5483	0.2419
5	✗	✗	✓	✓	0.7819	0.5684	0.7424	0.3075	0.4773	0.1275	0.6672	0.3344
6	✗	✓	✗	✓	0.6498	0.4412	0.5558	0.1896	0.4371	0.1182	0.5476	0.2497
7	✗	✓	✓	✗	0.7816	0.5582	0.8146	0.3291	0.5521	0.1424	0.7161	0.3432
8	✓	✗	✗	✓	0.6490	0.4416	0.5391	0.1779	0.4398	0.1172	0.5427	0.2456
9	✓	✗	✓	✗	0.7795	0.5614	0.8124	0.3316	0.5922	0.1556	0.7280	0.3495
10	✓	✓	✗	✗	0.6527	0.4440	0.5448	0.1811	0.4848	0.1277	0.5608	0.2510
11	✗	✓	✓	✓	0.7814	0.5653	0.8142	0.3235	0.5814	0.1477	0.7256	0.3455
12	✓	✗	✓	✓	0.7748	0.5564	0.8082	0.3254	0.5952	0.1549	0.7261	0.3456
13	✓	✓	✗	✓	0.6497	0.4407	0.5283	0.1666	0.4487	0.1161	0.5422	0.2411
14	✓	✓	✓	✗	0.7753	0.5516	0.8100	0.3251	0.5946	0.1480	0.7266	0.3416
LEFT	✓	✓	✓	✓	0.7836	0.5701	0.8157	0.3342	0.6562	0.1726	0.7518	0.3590

Table A4: Fusion strategy ablation. The best ones are in bold.

Training time represents the time cost to train the model for each epoch with batch size 128, while inference time indicates the duration required to process 128 samples.

Dataset	Fusion Method	VUS-ROC	VUS-PR	Training Time (s)	Inference Time (s)
PSM	$M \leftrightarrow F \leftrightarrow T$	0.7860	0.5692	30.29	0.01699
	$M \leftrightarrow F$	0.7687	0.5479	20.56	0.01080
	$M \leftrightarrow T$	0.7558	0.5371	18.93	0.01060
	$T \leftrightarrow F$	0.7790	0.5593	18.79	0.01066
	Default	0.7836	0.5701	25.66	0.01527
MSL	$M \leftrightarrow F \leftrightarrow T$	0.8106	0.3246	7.65	0.00854
	$M \leftrightarrow F$	0.8069	0.3255	6.62	0.00788
	$M \leftrightarrow T$	0.8051	0.3149	6.31	0.00787
	$T \leftrightarrow F$	0.8121	0.3265	6.46	0.00782
	Default	0.8157	0.3342	7.02	0.00841
SMAP	$M \leftrightarrow F \leftrightarrow T$	0.4776	0.1295	17.71	0.00854
	$M \leftrightarrow F$	0.5640	0.1419	15.40	0.00790
	$M \leftrightarrow T$	0.4330	0.1163	14.62	0.00788
	$T \leftrightarrow F$	0.6203	0.1634	15.50	0.00854
	Default	0.6562	0.1726	16.34	0.00856

A.8 Multi-scale Kernels Sensitivity

Fig. A3 shows that the choice of multi-scale kernels has a clear impact on performance. The VUS-ROC and VUS-PR results reported in Table 1 are obtained using kernel sizes (e.g. SMAP: (16, 8, 4)), which may not be optimal. A more thorough hyperparameter search over kernel settings could further improve the results.

A.9 Visualization

Fig. A4 illustrates qualitative results on PSM, MSL, and SMAP. CrossAD assigns elevated anomaly scores to many normal timestamps, so it produces frequent off-interval alarms and a high false positive rate. LEFT concentrates high scores around the annotated

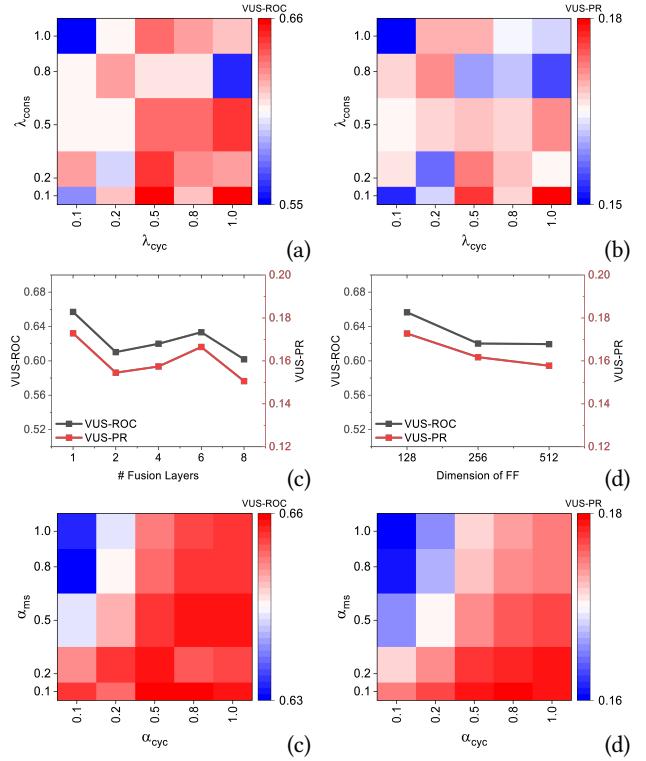


Figure A2: Fusion hyper-parameters sensitivity analysis on the SMAP dataset. (a) and (b) show the sensitivity to λ_{cyc} and λ_{cons} . (c) and (d) present the depth and width analysis. (e) and (f): α_{cyc} and α_{ms} sensitivity.

anomalous intervals, which reduces false alarms and improves

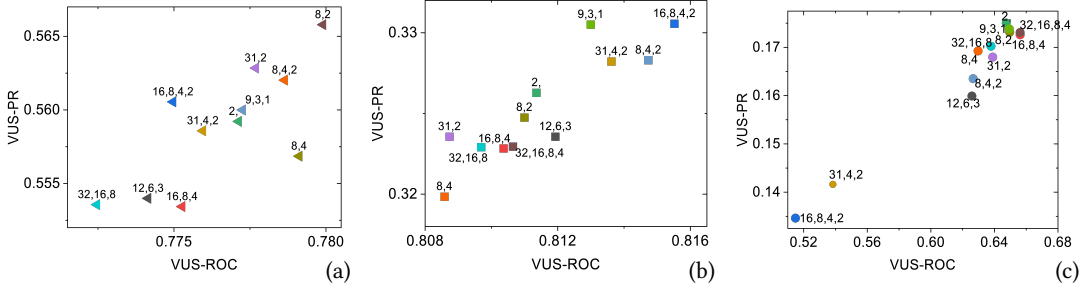


Figure A3: Multi-scale kernels sensitivity. (a): PSM. (b): MSL. (c): SMAP.

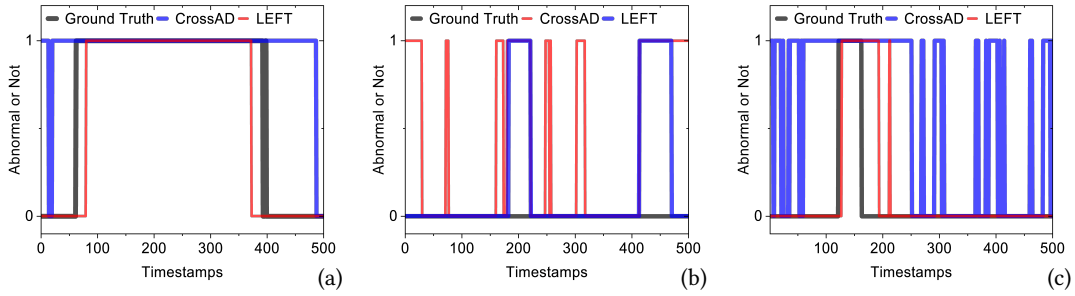


Figure A4: Example anomaly detection visualization. (a): PSM. (b): MSL. (c): SMAP. '1' denotes abnormal.

event-level precision. Overall, the cases reflect the same ranking trend measured by VUS-ROC and VUS-PR.

A.10 Details of the Proof

Proof of Lemma 3.1.

PROOF. Since $\sigma(u_k) \in (0, 1)$, $e_k - e_{k-1} = (c_k - e_{k-1})\sigma(u_k) \geq 0$, hence edges are monotone, and $e_k \leq e_{k-1} + (c_k - e_{k-1}) = c_k$.

Downsampling repeats the spectrum and overlaps these copies. As a result the aliasing mainly comes from the remaining energy above the cutoff frequency c_k , scaled by $\vartheta(r_k)$,

$$\|\Delta_{r_k}(X^{(k)})\|_2 \leq \vartheta(r_k) \sum_{f > c_k} \|\tilde{X}^{(k)}(f)\|_2. \quad (38)$$

Using $\tilde{X}^{(k)}(f) = \tilde{m}_k(f)\tilde{X}(f)$ and Cauchy-Schwarz,

$$\sum_{f > c_k} \|\tilde{X}^{(k)}(f)\|_2 \leq \|\tilde{X}\|_2 \sum_{f > c_k} \tilde{m}_k(f) = \|\tilde{X}\|_2 \epsilon_k, \quad (39)$$

where we used $0 \leq \tilde{m}_k(f) \leq 1$. Substituting yields (4).

□

Proof of Lemma 3.2.

PROOF. By definition,

$$\hat{S}_{\rightarrow f} - S = W_\theta(\hat{X}) - W_\theta(X) = W_\theta(\hat{X} - X). \quad (40)$$

Applying (20) to $Y = \hat{X} - X$ gives,

$$\sqrt{A} \|\hat{X} - X\|_2 \leq \|\hat{S}_{\rightarrow f} - S\|_2 \leq \sqrt{B} \|\hat{X} - X\|_2, \quad (41)$$

which yields (21) and (22).

□

Proof of Lemma 3.3.

PROOF. We repeatedly use the elementary inequality for SmoothL1: for any scalar residual r ,

$$|r| \leq 2l(r, 0) + 1, \quad (42)$$

which implies the same inequality after averaging over entries.

(1) **Bounding the multi-scale score by \mathcal{L}_{ms} .** $\mathcal{A}_{\text{ms}}(t)$ is a weighted sum of absolute reconstruction residuals aggregated across supervised scales. Applying (42) element-wise to each supervised residual and absorbing fixed dimensional factors yields,

$$\langle \mathcal{A}_{\text{ms}}(t) \rangle_t \leq \kappa_{\text{ms}} \mathcal{L}_{\text{ms}} + \kappa_0^{(1)}. \quad (43)$$

(2) **Bounding the raw cycle magnitude by \mathcal{L}_{cyc} and $\mathcal{L}_{\text{cons}}$.** By definition, $\mathcal{A}_{\text{cyc}}(t) = (\text{MA}_k(\tilde{\mathcal{A}}_{\text{cyc}}))(t)$ with $\tilde{\mathcal{A}}_{\text{cyc}}(t) \geq 0$.

The term $|\hat{X}_{\leftarrow f} - X|$ is directly controlled by the time-domain SmoothL1 term $l(\hat{X}_{\leftarrow f}, X)$ in \mathcal{L}_{cyc} via (42).

For $|\hat{X} - X|$, Lemma 3.2 gives $\|\hat{X} - X\|_2 \leq \frac{1}{\sqrt{A}} \|\hat{S}_{\rightarrow f} - S\|_2$. Standard norm relations convert this to a bound on the mean absolute residual up to a fixed constant, and $\|\hat{S}_{\rightarrow f} - S\|_2$ is controlled by the spectral SmoothL1 term $l(\hat{S}_{\rightarrow f}, S)$ in \mathcal{L}_{cyc} via (42). Hence,

$$\alpha_f \langle |\hat{X}_{\leftarrow f} - X| \rangle_t + \alpha_t \langle |\hat{X} - X| \rangle_t \leq \kappa_{\text{cyc}} \mathcal{L}_{\text{cyc}} + \kappa_0^{(2)}. \quad (44)$$

For the cross-path term, using the definition $c(t) = |\hat{X}_{\text{ms}}(t) - \hat{X}_{\leftarrow f}(t)|$ and applying (42) to $l(\hat{X}_{\text{ms}}, \hat{X}_{\leftarrow f}) = \mathcal{L}_{\text{cons}}$ gives,

$$\alpha_c \langle c(t) \rangle_t \leq \kappa_{\text{cons}} \mathcal{L}_{\text{cons}} + \kappa_0^{(3)}. \quad (45)$$

Combining the above with the nonnegative gate term yields,

$$\langle \tilde{\mathcal{A}}_{\text{cyc}}(t) \rangle_t \leq \kappa_{\text{cyc}} \mathcal{L}_{\text{cyc}} + \kappa_{\text{cons}} \mathcal{L}_{\text{cons}} + \kappa_g \alpha_g \langle |g(t)| \rangle_t + \kappa_0^{(4)}. \quad (46)$$

Applying (30) with $u(t) = \tilde{\mathcal{A}}_{\text{cyc}}(t)$ yields,

$$\langle \mathcal{A}_{\text{cyc}}(t) \rangle_t \leq \rho_\kappa \left(\kappa_{\text{cyc}} \mathcal{L}_{\text{cyc}} + \kappa_{\text{cons}} \mathcal{L}_{\text{cons}} + \kappa_g \alpha_g \langle |g(t)| \rangle_t + \kappa_0^{(4)} \right). \quad (47)$$

(3) Combining to obtain the normal-window upper bound.

Using $\mathcal{A}(t) = \alpha_{\text{cyc}} \mathcal{A}_{\text{cyc}}(t) + \alpha_{\text{ms}} \mathcal{A}_{\text{ms}}(t)$, absorbing fixed coefficients into κ_{ms} , κ_{cyc} , κ_{cons} , and substituting $\mathcal{L}_{\text{ms}} \leq \varepsilon_{\text{ms}}$, $\mathcal{L}_{\text{cyc}} \leq \varepsilon_{\text{cyc}}$, $\mathcal{L}_{\text{cons}} \leq \varepsilon_{\text{cons}}$ gives (32).

(4) Lower bounds on anomalous segments. Under the stated conditions on Ω and nonnegativity of all terms,

$$\begin{aligned} \langle \tilde{\mathcal{A}}_{\text{cyc}}(t) \rangle_{t \in \Omega} &\geq \alpha_t \langle |\hat{X}(t) - X(t)| \rangle_{t \in \Omega} + \alpha_f \langle |\hat{X}_{\leftarrow f}(t) - X(t)| \rangle_{t \in \Omega} + \alpha_c \langle c(t) \rangle_{t \in \Omega} \\ &\geq \alpha_t \delta_t + \alpha_f \delta_f + \alpha_c \delta_c, \end{aligned} \quad (48)$$

which yields (33). If the pointwise bounds hold and the averaging window lies in Ω , then $\mathcal{A}_{\text{cyc}}(t) = \text{MA}_\kappa(\tilde{\mathcal{A}}_{\text{cyc}})(t)$ preserves the same lower bound.

For prototype inconsistency, Pinsker's inequality implies $\text{JS}(p, q) \geq \frac{1}{8} \|p - q\|_1^2$ for any distributions p, q , hence $d(t) \geq \frac{1}{8} \delta_p^2$ on Ω and (34) follows. \square